molecules

MDPI

Article

A Cell-Penetrating Peptide Modified $Cu_{2-x}Se$/Au Nanohybrid with Enhanced Efficacy for Combined Radio-Photothermal Therapy

Ruixue Ran [1,†], Sinan Guo [1,†], Xiaoyu Jiang [1], Zhanyin Qian [1], Zhaoyang Guo [1], Yinsong Wang [1], Mingxin Cao [2,*] and Xiaoying Yang [1,*]

[1] Tianjin Key Laboratory of Technologies Enabling Development of Clinical Therapeutics and Diagnostics (Theranostics), School of Pharmacy, Tianjin Medical University, Tianjin 300070, China
[2] School and Hospital of Stomatology, Tianjin Medical University, Tianjin 300070, China
* Correspondence: mingxincao@tmu.edu.cn (M.C.); yangxiaoying@tmu.edu.cn (X.Y.)
† These authors contributed equally to this work.

Abstract: Radiotherapy (RT) is one of the main clinical therapeutic strategies against cancer. Currently, multiple radiosensitizers aimed at enhancing X-ray absorption in cancer tissues have been developed, while limitations still exist for their further applications, such as poor cellular uptake, hypoxia-induced radioresistance, and unavoidable damage to adjacent normal body tissues. In order to address these problems, a cell-penetrating TAT peptide (YGRKKRRQRRRC)-modified nanohybrid was constructed by doping high-Z element Au in hollow semiconductor $Cu_{2-x}Se$ nanoparticles for combined RT and photothermal therapy (PTT) against breast cancer. The obtained $Cu_{2-x}Se$ nanoparticles possessed excellent radiosensitizing properties based on their particular band structures, and high photothermal conversion efficiency beneficial for tumor ablation and promoting RT efficacy. Further doping high-Z element Au deposited more high-energy radiation for better radiosensitizing performance. Conjugation of TAT peptides outside the constructed $Cu_{2-x}Se$/Au nanoparticles facilitated their cellular uptake, thus reducing overdosage-induced side effects. This prepared multifunctional nanohybrid showed powerful suppression effects towards breast cancer, both in vitro and in vivo via integrating enhanced cell penetration and uptake, and combined RT/PTT strategies.

Keywords: radiosensitizer; TAT peptide; radiotherapy; photothermal therapy; combined therapy

check for updates

Citation: Ran, R.; Guo, S.; Jiang, X.; Qian, Z.; Guo, Z.; Wang, Y.; Cao, M.; Yang, X. A Cell-Penetrating Peptide Modified $Cu_{2-x}Se$/Au Nanohybrid with Enhanced Efficacy for Combined Radio-Photothermal Therapy. *Molecules* **2023**, *28*, 423. https://doi.org/10.3390/molecules28010423

Academic Editors: Yanyan Jiang and Xijian Liu

Received: 19 November 2022
Revised: 24 December 2022
Accepted: 29 December 2022
Published: 3 January 2023

Copyright: © 2023 by the authors. Licensee MDPI, Basel, Switzerland. This article is an open access article distributed under the terms and conditions of the Creative Commons Attribution (CC BY) license (https://creativecommons.org/licenses/by/4.0/).

1. Introduction

Cancer has been the chief reason of death worldwide. Among primary therapeutic strategies, radiotherapy (RT) is a powerful one used for over a century, which noninvasively exerts tumoricidal effects by damaging DNA directly and generating cytotoxic reactive oxygen species (ROS) indirectly [1,2]. However, X-ray irradiation alone faces multiple challenges, such as the inevitable harms to neighboring normal tissues and radioresistance induced by tumor hypoxia [3,4]. Various radiosensitizers aimed at enhancing X-ray absorption in tissues have been developed, and it is essential for them to establish the properties of stability, good biocompatibility, and tumor targeted delivery and uptake for effective clinical practice. With the development of nanotechnology, nanoparticle radiosensitizers provide versatile strategies in order to deal with these problems [5]. Among them, high-Z elements (e.g., Au [6,7], Hf [8,9], Bi [10,11], and Gd [12])-containing nanoparticles can effectively absorb high-energy radiation, and therefore can be employed as radiosensitizers to heighten the response of tumor cells to radiation. Furthermore, semiconductor nanoparticles, such as Bi_2Se_3 [13], WS_2 [14], Bi_2S_3 [15], and $Cu_{2-x}Se$ [16], have also been extensively explored as radiosensitizers and can generate ROS based on their particular band structures.

Another essential treatment strategy for improving RT efficacy is combining useful therapies with RT for synergistic effects [1]. PTT has been reported to be one of the most effective candidates for RT combination therapeutics [17,18]. By using photothermal agents absorbed in the near-infrared (NIR) range, PTT can transform NIR luminous energy into thermal energy for tumor ablation [19]. On one hand, hyperthermia induced during PTT can elevate radiosensitivity via increasing intratumoral blood flow, and thus enhance the oxygenation status and reverse hypoxia-induced radioresistance [20]. Additionally, hyperthermia results in double strand DNA breaks, preventing DNA repair after RT [21]. Furthermore, hyperthermia can kill radiation-insensitive cancer cells of the S-phase to raise the productivity of radiotherapy [22]. On the other hand, RT can compensate for the incomplete ablation of deep-seated tumors by NIR light, owing to its higher penetration ability [23]. Therefore, nanomaterials with both photothermal ablation and radiosensitizing properties are promising for improving therapeutic outcome.

Semiconductor $Cu_{2-x}Se$ ($0 \leq x \leq 1$) nanoparticles are ideal in RT and PTT combination therapeutics because of their radiosensitizing properties and high photothermal conversion efficiency acting as PTT agents [16,24–26]. Furthermore, the role of Cu and Se as important human trace elements confers $Cu_{2-x}Se$ nanoparticles satisfactory biocompatibility [27,28]. Chemically doping high-Z element Au in $Cu_{2-x}Se$ nanoparticles could deposit more energy for better radiosensitizing performance. Thus, we considered applying nanohybrids of $Cu_{2-x}Se$/Au nanoparticles, hoping to acquire the synergistic effects of radiosensitizing and photothermal ablation.

As mentioned above, except for elevating radiosensitivity, ensuring the efficient delivery and cellular uptake in vivo is also vital for exerting their anticancer effects and preventing possible harms to normal tissues. Cell-penetrating peptides (CPPs), one of the most effective positive-charged modifications on nanomaterials, have been widely used in cell membrane infiltration and cellular internalization based on the electrostatic adsorption capacity of negative-charged cancer cell membranes [29,30]. Among them, TAT peptide is a classic one that can easily diffuse across cell membranes [31]. Our previous study modified TAT on surface of nanoparticles for breast cancer treatment, and in vitro/in vivo outcomes certificated evidently increased cellular internalization and nuclear localization mediated by TAT peptide [32]. Therefore, it is promising to design $Cu_{2-x}Se$/Au nanoparticles with TAT peptide to enhance cellular uptake and avoid harmful radiation dosage for the highest therapeutic efficacy.

Herein, TAT-modified $Cu_{2-x}Se$/Au nanoparticles ($Cu_{2-x}Se$/Au-TAT nanoparticles) with uniform size and morphology were developed, exhibiting satisfactory radiosensitizing effect and photothermal performance suitable for cancer RT/PTT combination therapy. As illustrated in Scheme 1A, hollow $Cu_{2-x}Se$ nanoparticles were prepared via the sacrificial template method by using Cu_2O nanoparticles as the sacrificial templates, and $Cu_{2-x}Se$/Au nanoparticles were synthesized via in situ growing Au on $Cu_{2-x}Se$ nanoparticles. To strengthen the cellular uptake ability and therapeutic effects, TAT peptide was used to modify $Cu_{2-x}Se$/Au nanoparticles. The combined RT/PTT effects of $Cu_{2-x}Se$/Au-TAT nanoparticles against breast cancer are proposed in Scheme 1B. After intratumoral injection, $Cu_{2-x}Se$/Au-TAT nanoparticles can be taken up by breast cancer cells efficiently mediated by TAT peptide. Upon NIR laser irradiation, $Cu_{2-x}Se$ nanoparticles exert photothermal performance to ablate tumor via hyperthermia. Meanwhile, increased intratumoral blood flow induced by hyperthermia leads to improved oxygenation level, thus heightening the sensitivity of hypoxic tumor cells to RT. After exposure to X-ray irradiation, abundant high-Z element Au in $Cu_{2-x}Se$/Au-TAT nanoparticles can deposit higher radiation energy within tumor to damage DNA, at the same time aiding $Cu_{2-x}Se$ nanoparticles to promote the generation of more cytotoxic ROS. Moreover, the constructed hollow nanostructure holds the potential to act as carriers for multifunctional agents, such as chemotherapeutic drugs [33], photosensitizer [34], photothermal agents [35], and so on, further expanding its application. Thus, this work highlights an excellent multifunctional nanoplatform based on $Cu_{2-x}Se$/Au-TAT nanoparticles for combined RT/PTT therapy.

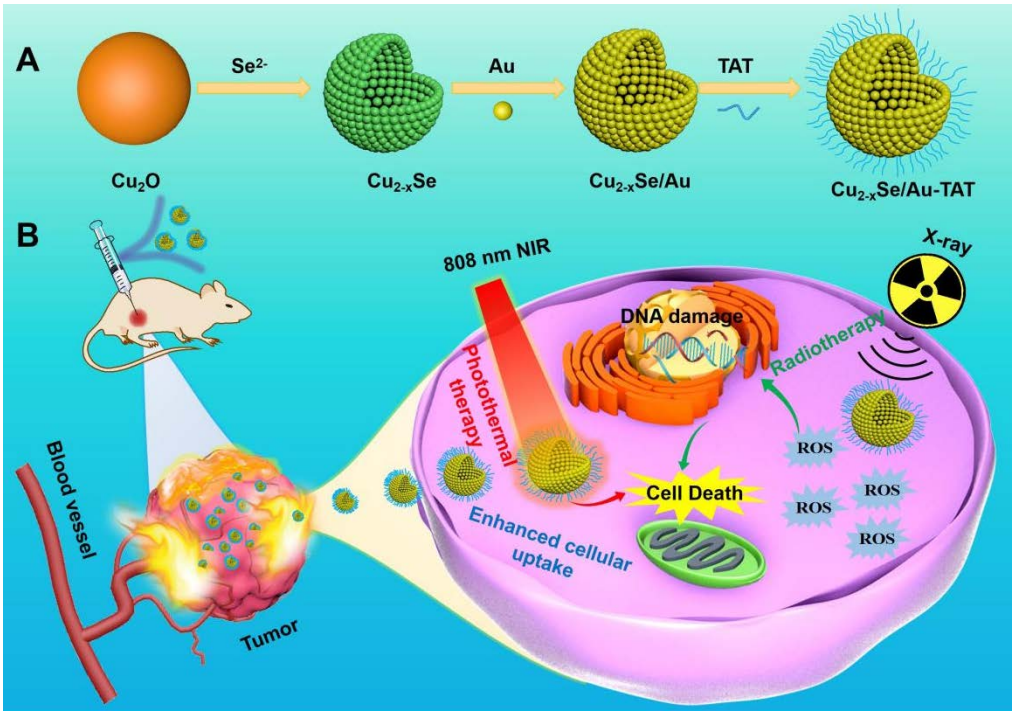

Scheme 1. (**A**) Synthesis of $Cu_{2-x}Se$/Au-TAT nanoparticles; (**B**) Schematic illustration of $Cu_{2-x}Se$/Au-TAT nanoparticles for RT/PTT combination therapy.

2. Results and Discussion

2.1. Synthesis and Characterization of $Cu_{2-x}Se$/Au-TAT Nanoparticles

The synthesis process of $Cu_{2-x}Se$/Au-TAT nanoparticles is shown in Scheme 1A. $Cu_{2-x}Se$/Au-TAT nanoparticles were synthesized via a multistep synthesis process. Briefly, in the presence of polyvinylpyrrolidone (PVP), Cu_2O nanoparticles were synthesized by reducing copper chloride dihydrate ($CuCl_2{\cdot}2H_2O$) with hydrazine hydrate ($N_2H_4{\cdot}H_2O$). Then, $Cu_{2-x}Se$ nanoparticles were prepared by a sacrificial template method with Cu_2O nanoparticles as the sacrificial template and selenium powder as the selenium source. Afterward, $Cu_{2-x}Se$/Au nanoparticles were prepared through a spontaneous redox process using hydrogen tetrachloroaurate ($HAuCl_4$) as the source of Au. Finally, TAT was modified on the surface to improve the cellular uptake. Transmission electron microscopy (TEM) was employed to study the characteristics of size and morphology of the nanomaterials. As illustrated in Figure 1A, Cu_2O nanoparticles were solid spheroids with an average size of 95 ± 5 nm, while $Cu_{2-x}Se$ nanoparticles maintained the spherical morphology with a hollow structure (136 ± 3 nm) (Figure 1B). After in situ deposition of Au on the surface of $Cu_{2-x}Se$ nanoparticles, the average particle sizes of $Cu_{2-x}Se$/Au nanoparticles (154 ± 6 nm) increased compared with $Cu_{2-x}Se$ nanoparticle (Figure 1C). After surface modification with TAT, the generated $Cu_{2-x}Se$/Au-TAT nanoparticles exhibited increased surface roughness (Figure 1D). The composition of nanoparticles was further verified by elemental mapping. From Figure 1E, it is clearly displayed that $Cu_{2-x}Se$/Au nanoparticles contained Cu, Se, and Au, and the Au element was evenly distributed on the $Cu_{2-x}Se$ nanoparticles. According to the dynamic light scattering (DLS) assessment, compared with the particle size of $Cu_{2-x}Se$/Au, the size of the final $Cu_{2-x}Se$/Au-TAT increased slightly to 154 ± 6 nm (Figure 1F). As illustrated in Figure 1G, the zeta potentials of Cu_2O, $Cu_{2-x}Se$, and $Cu_{2-x}Se$/Au nanoparticles were −9.3 ± 0.6, −18.4 ± 0.8, and −12.9 ± 0.7 mV, respectively, while the zeta potential of $Cu_{2-x}Se$/Au-TAT nanoparticles was reversed to +25.1 ± 1.8 mV after surface modification with TAT. The results further clarified the successful introduction of TAT on $Cu_{2-x}Se$/Au nanoparticles. The stability of $Cu_{2-x}Se$/Au-TAT nanoparticles in aqueous solution was also detected by DLS, as demonstrated in Figure 1H;

the minor variation in the hydrodynamic size in 5 days indicated $Cu_{2-x}Se$/Au-TAT nanoparticles had a good stability.

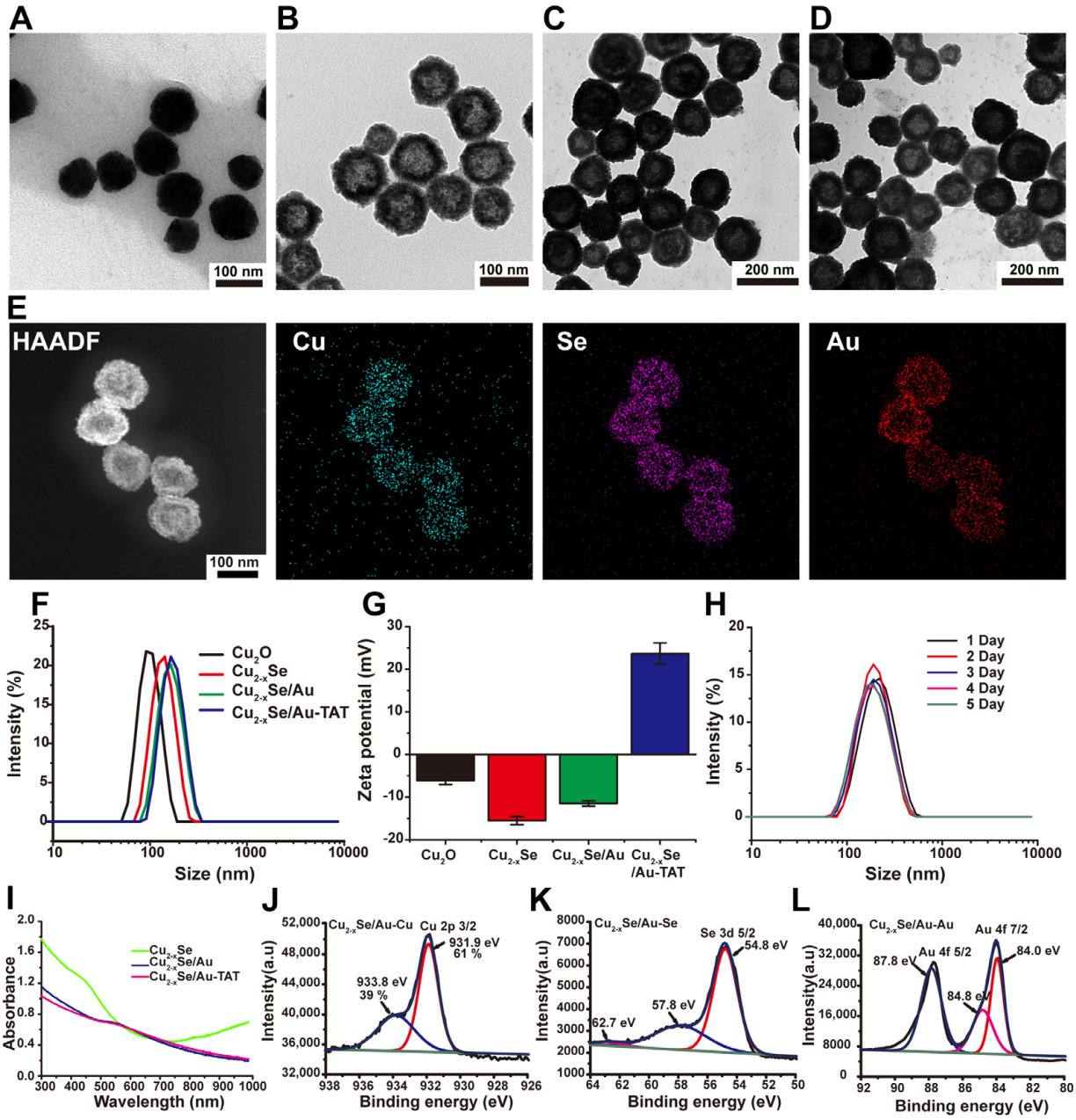

Figure 1. Characterization of $Cu_{2-x}Se$/Au-TAT nanoparticles. TEM images of (**A**) Cu_2O nanoparticles, (**B**) $Cu_{2-x}Se$ nanoparticles, (**C**) $Cu_{2-x}Se$/Au nanoparticles, and (**D**) $Cu_{2-x}Se$/Au-TAT nanoparticles; (**E**) Elemental mapping of $Cu_{2-x}Se$/Au nanoparticles, demonstrating the existence and ratio of Cu, Se, and Au; (**F**) Size distributions and (**G**) zeta potential of Cu_2O nanoparticles, $Cu_{2-x}Se$ nanoparticles, $Cu_{2-x}Se$/Au nanoparticles, and $Cu_{2-x}Se$/Au-TAT nanoparticles; (**H**) Variation of hydrodynamic size of $Cu_{2-x}Se$/Au-TAT nanoparticles in water over 5 days; (**I**) UV-vis-NIR spectra of $Cu_{2-x}Se$ nanoparticles, $Cu_{2-x}Se$/Au nanoparticles, and $Cu_{2-x}Se$/Au-TAT nanoparticles. XPS survey spectra of Cu (**J**), Se (**K**), and Au (**L**) of $Cu_{2-x}Se$/Au nanoparticles.

UV−vis−NIR spectra was utilized to study the optical features of different nanoparticles. Figure 1I shows that the strong localized surface plasmon resonance (LSPR) of $Cu_{2-x}Se$ nanomaterials was weakened after the formation of $Cu_{2-x}Se$/Au nanoparticles, and the absorption at about 560 nm that appeared in $Cu_{2-x}Se$/Au nanoparticles was attributed to

the LSPR of Au nanoparticles, which further proves that Au nanoparticles were effectively deposited on $Cu_{2-x}Se$ nanoparticles.

An X-ray photoelectron spectroscopy (XPS) analytical experiment was employed to study the valence states of elementary substances in $Cu_{2-x}Se$ nanoparticles and $Cu_{2-x}Se$/Au nanoparticles (Figure 1J–L and Figure S1). As shown in Figure S1C, the two strong peaks situated at 932.8 eV and 952.7 eV, accounting for 83%, corresponded to Cu $2p_{3/2}$ and Cu $2p_{1/2}$ of Cu (I), respectively, indicating that Cu (I) was the main valence state of $Cu_{2-x}Se$. While the two weak peaks located at 934.4 eV and 953.9 eV, accounting for 17%, corresponded to Cu $2p_{3/2}$ and Cu $2p_{1/2}$ of Cu (II), accordingly, demonstrating that Cu (II) also accounted for a small part of $Cu_{2-x}Se$. Moreover, the binding energy peak at 54.8 eV represents the characteristic Se 3d, corresponding to Se (II) (Figure S1D). As shown in Figure 1J for $Cu_{2-x}Se$/Au nanoparticles, the content of Cu (I) decreased to 61% and the content of Cu (II) increased to 39% compared with the content in $Cu_{2-x}Se$ nanoparticles, which proves that a part of Cu (I) was oxidized to Cu (II) during the generation process of $Cu_{2-x}Se$/Au nanoparticles. From Figure 1K and Figure S1D, it can be seen that the valence state of selenium does not change from $Cu_{2-x}Se$ to $Cu_{2-x}Se$/Au. The binding energy of Au $4f_{5/2}$ and $4f_{7/2}$ located at 87.8 eV and 84.0 eV were attributed to Au (0), which proves that Au (III) was reduced to Au (0) (Figure 1L). Further, the compositions of $Cu_{2-x}Se$ nanoparticles and $Cu_{2-x}Se$/Au nanoparticles were determined by an inductively coupled plasma optical emission spectrometer (ICP-OES). The Cu/Se atomic ratio in $Cu_{2-x}Se$ nanoparticles was 1.81:1, showing copper deficiency characteristics. The Cu/Se/Au atomic ratio in $Cu_{2-x}Se$/Au nanoparticles is 0.48:1:0.51. The reduction of Cu/Se ratio in $Cu_{2-x}Se$/Au nanoparticles further supported the reduction of Au (III) by Cu (I) in the XPS results. All of the above results clarify the spontaneous redox process from $Cu_{2-x}Se$ nanoparticles to $Cu_{2-x}Se$/Au nanoparticles after the addition of $HAuCl_4$ solution into $Cu_{2-x}Se$ nanoparticles.

2.2. Photothermal and Radiosensitizing Performances of $Cu_{2-x}Se$/Au-TAT Nanoparticles

$Cu_{2-x}Se$ nanoparticles can be utilized as efficient photothermal agents thanks to the characteristic of strong LSPR in the region of NIR [16,24–26]. The photothermal features of $Cu_{2-x}Se$/Au-TAT nanoparticles were researched by photothermal conversion tests. As visually illustrated in Figure 2A, after the solution of $Cu_{2-x}Se$/Au-TAT nanoparticles (80 μg/mL) being performed with a 10-min 808 nm irradiation at 0.5, 1.0, and 1.5 W/cm^2, the temperatures of the solutions increased to 45 °C, 53 °C, and 58 °C, respectively, which indicates that the increase in temperature had positive noteworthy correlation with irradiation dose. The increase in temperature in solutions of $Cu_{2-x}Se$/Au-TAT nanoparticles also presented a concentration-dependent manner (Figure 2B). As visually displayed in Figure 2F, the temperature of $Cu_{2-x}Se$/Au-TAT nanoparticles could increase to 53 °C under a 10-min irradiation at 1.0 W/cm^2, while it was difficult for the water temperature to go up, showing that $Cu_{2-x}Se$/Au-TAT nanoparticles had excellent photothermal properties. According to previous literature, NIR-triggered photothermal therapy usually requires hyperthermia of >50 °C to achieve the thorough ablation of tumor [36], while extremely higher temperatures could damage normal cells. For this reason, $Cu_{2-x}Se$/Au-TAT nanoparticles at the concentration of 80 μg/mL under a 10-min laser irradiation at 1.0 W/cm^2 were chose for the conditions of evaluating the subsequent photothermal ablation effects towards cancer cells. Moreover, the photothermal stability of $Cu_{2-x}Se$/Au-TAT nanoparticles was studied by NIR laser irradiation repeatedly for 5 cycles (Figure 2C), and the decrease in peak value of temperature with the addition of cycle was ignorable, indicating excellent photothermal stability. According to the equations listed in the Materials and Methods section, the time constant (τ) was 328.96 s (Figure 2D,E), and the photothermal conversion efficiency (η) of $Cu_{2-x}Se$/Au-TAT was approximately 64.6%, determined by a previously reported method [37]. The photothermal conversion efficiency of $Cu_{2-x}Se$/Au-TAT is higher than some inorganic nanoparticles, such as CuO@AuCu-TPP (37.9%) [38], hollow Cu_2Se nanozymes (50.9%) [39], and many organic nanoparticles, such as polypyrrole nanoparticles (22.6%) [40] and polydopamine-contained hydrogel (45.7%) [37].

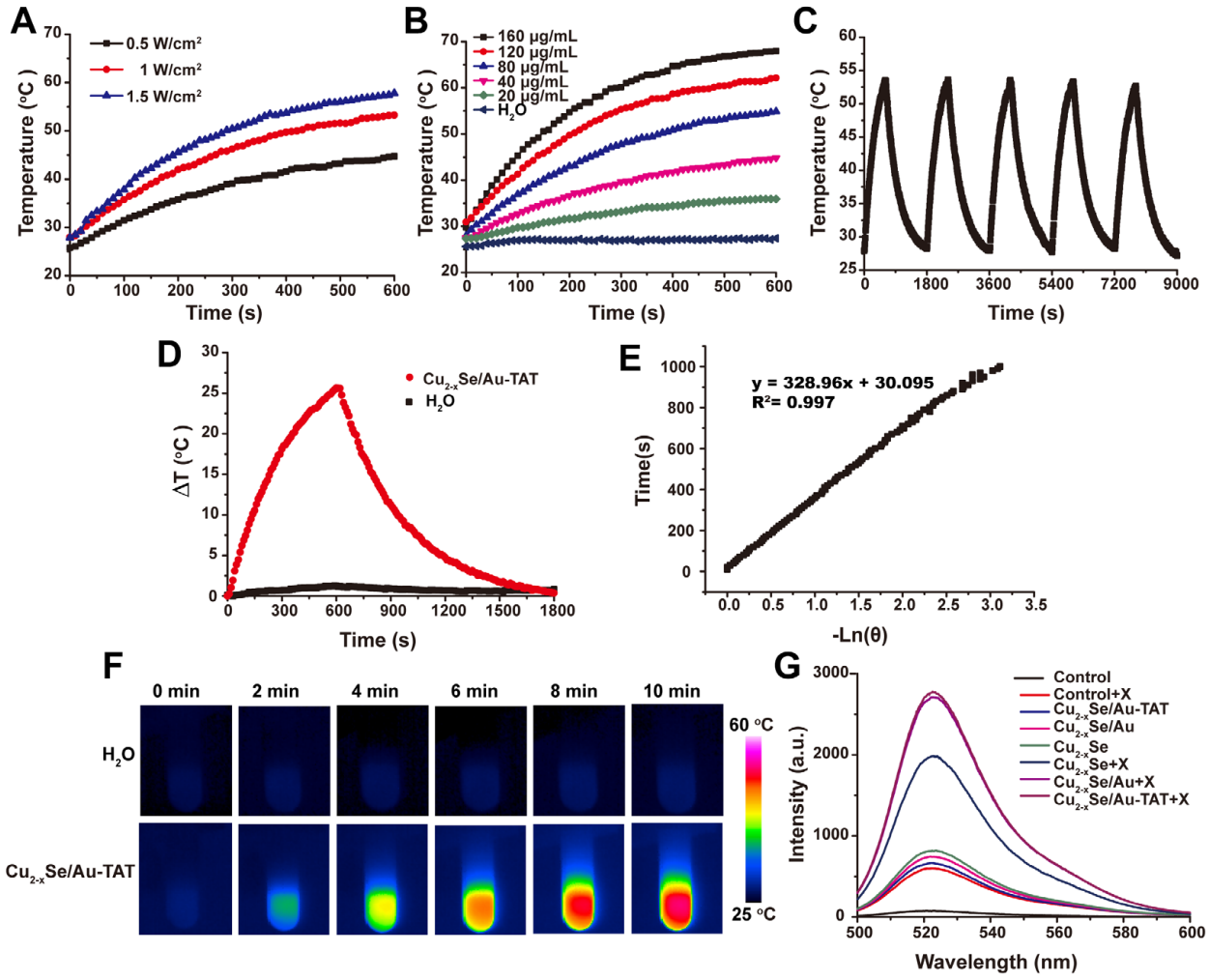

Figure 2. Evaluation of photothermal performance of $Cu_{2-x}Se$/Au-TAT nanoparticles under an 808 nm laser. (**A**) Temperature changes of $Cu_{2-x}Se$/Au-TAT nanoparticles (80 μg/mL) with the powers of 0.5, 1.0, and 1.5 W/cm^2, correspondingly; (**B**) Photothermal heating curves of $Cu_{2-x}Se$/Au-TAT nanoparticles with various concentrations (0, 20, 40, 80, 120, and 160 μg/mL) at 1.0 W/cm^2; (**C**) Heating curves of $Cu_{2-x}Se$/Au-TAT nanoparticles (80 μg/mL) at 1.0 W/cm^2 by laser ON/OFF assays for 5 cycles; (**D**) Heating and cooling curves of $Cu_{2-x}Se$/Au-TAT and H_2O upon 808 nm laser irradiation (1 W/cm^2). (**E**) Linear time data versus -Ln θ obtained from the cooling period of Figure 2D. (**F**) Thermal images of water and $Cu_{2-x}Se$/Au-TAT nanoparticles (80 μg/mL) with the power of 1.0 W/cm^2 at indicated time; (**G**) Fluorescence intensities of DCF in the solutions of multiple nanoparticles with or without performing X-ray irradiation.

Previous literatures had shown that the high-Z element and semiconductor heterostructures endow nanomaterials with better radiosensitization performance than high-Z element or semiconductor alone [26,41]. In order to verify the radiosensitization of $Cu_{2-x}Se$/Au-TAT nanoparticles, ROS generation in solution was investigated by using a probe compound 2,7-dichlorodihydrofluorescein diacetate (DCFH-DA). As can be demonstrated from Figure 2G, the fluorescence intensity of the group of $Cu_{2-x}Se$ + RT was largely higher than control + RT, while the fluorescence intensities observed in the group of $Cu_{2-x}Se$/Au + RT and $Cu_{2-x}Se$/Au-TAT + RT were higher compared to those in the $Cu_{2-x}Se$+RT group, which indicated that high-Z element Au and semiconductor $Cu_{2-x}Se$ both played important roles in promoting the production of ROS.

2.3. Biocompatibility and Cellular Uptake of $Cu_{2-x}Se$/Au-TAT Nanoparticles

The cellular uptake of $Cu_{2-x}Se$/Au-TAT nanoparticles in mouse triple-negative breast cancer cell line (4T1) were investigated firstly. As demonstrated in Figure 3A, compared with the free fluorescein isothiocyanate (FITC)-treated group, the obvious fluorescent signals have been observed in both FITC-labeled $Cu_{2-x}Se$/Au-TAT- and $Cu_{2-x}Se$/Au-treated groups, and the fluorescent signal in the FITC-labeled $Cu_{2-x}Se$/Au-TAT-treated group was the strongest, indicating that the modification of TAT could enhance the uptake of $Cu_{2-x}Se$/Au. Next, a 3-(4,5-dimethyl-2-thiazolyl)-2,5-diphenyl-2-H-tetrazolium bromide (MTT) experiment was employed to test the cytotoxicity of $Cu_{2-x}Se$/Au-TAT nanoparticles in 4T1 and human umbilical vein endothelial cell lines (HUVECs). As can be seen from Figure 3B, the cell survival rate of 4T1 and HUVECs cells were still above 80%, though the concentration of $Cu_{2-x}Se$/Au-TAT nanoparticles was raised to 120 μg/mL, which demonstrates that the nanoparticles had little cytotoxicity within this concentration range, which lays a good foundation for further experiments.

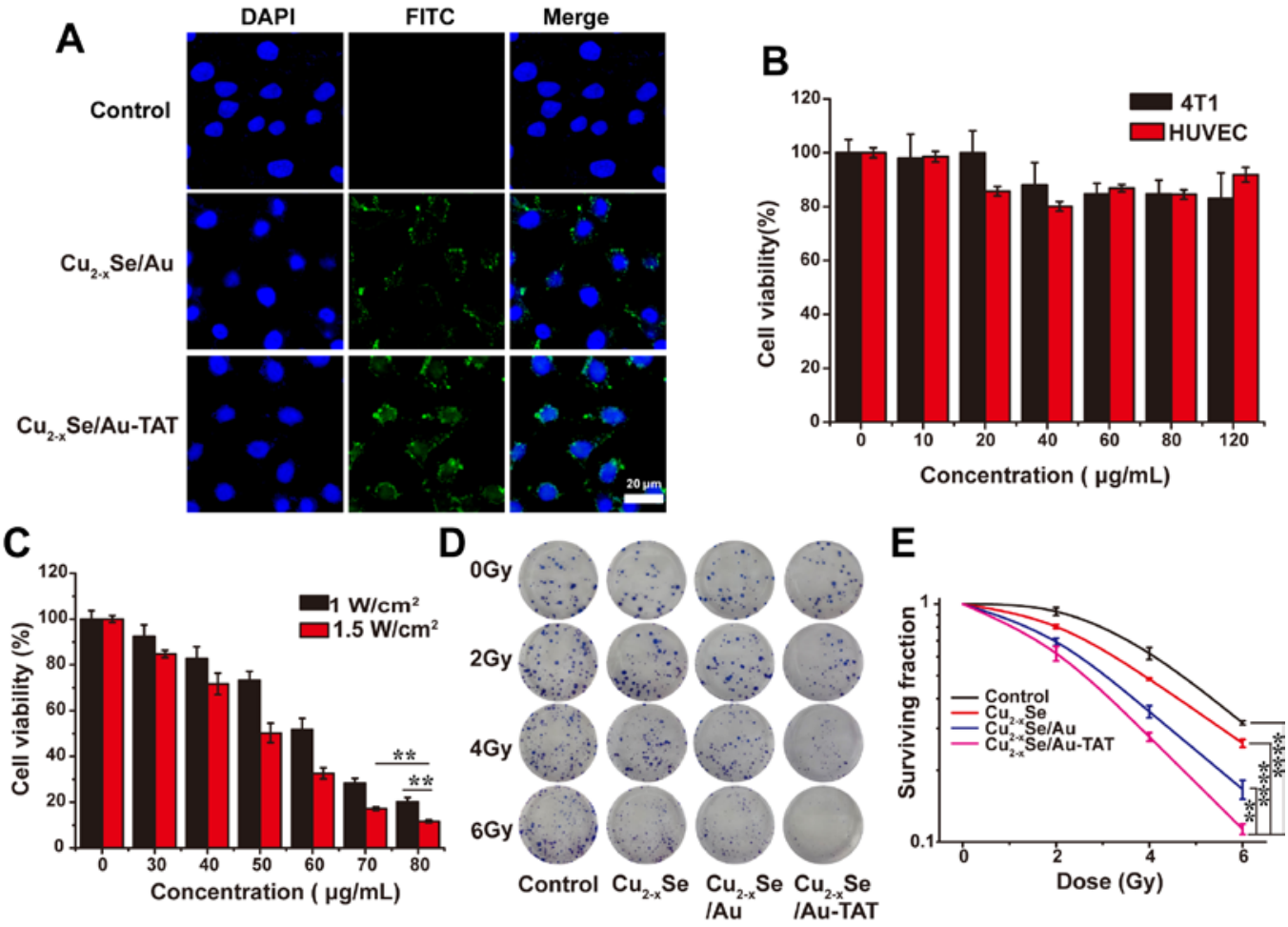

Figure 3. (**A**) Confocal fluorescent photos of 4T1 cells incubated with FITC, FITC−$Cu_{2-x}Se$/Au, and FITC-$Cu_{2-x}Se$/Au-TAT for 4 h; (**B**) Cell viabilities of 4T1 and HUVEC cells after incubation with $Cu_{2-x}Se$/Au-TAT nanoparticles at multiple concentrations (10, 20, 40, 60, 80, and 120 μg/mL); (**C**) Cell survival rate of 4T1 cells after co-culturing with $Cu_{2-x}Se$/Au-TAT nanoparticles at different concentrations (30, 40, 50, 60, 70, and 80 μg/mL) with an 808 nm NIR laser at a power density of 1.0 and 1.5 W/cm^2 for 10 min; (**D**) Clonogenic assay and (**E**) Clonogenic survival assay of 4T1 processed with control (PBS), $Cu_{2-x}Se$, $Cu_{2-x}Se$/Au, and $Cu_{2-x}Se$/Au-TAT nanoparticles at 0, 2, 4, and 6 Gy. *p* values were computed by the Student's *t*-test: ** $p < 0.01$, **** $p < 0.0001$.

2.4. Photothermal Ablation and Radiosensitization Effects In Vitro

The photothermal behavior and radiosensitization effects of $Cu_{2-x}Se$/Au-TAT nanoparticles were further investigated on 4T1 cells. As can been seen in Figure 3C, the antitumor efficacy of $Cu_{2-x}Se$/Au-TAT nanoparticles demonstrated an obvious concentration-dependent way after carrying out an irradiation by 808 nm light. The cell survival rate reduced with the rise of concentrations of $Cu_{2-x}Se$/Au-TAT nanoparticles, and the survival rate was only 50% after being cultured with 60 μg/mL $Cu_{2-x}Se$/Au-TAT nanoparticles at 1.0 W/cm^2 or 50 μg/mL at 1.5 W/cm^2. Cell viability even decreased to 80% at 1.0 W/cm^2 or 88% at 1.5 W/cm^2 at 80 μg/mL. The above results demonstrate that $Cu_{2-x}Se$/Au-TAT nanoparticles exhibited excellent photothermal conversion properties and could be used to ablate tumor cells in vitro.

Figure 2E has already shown that $Cu_{2-x}Se$, $Cu_{2-x}Se$/Au, and $Cu_{2-x}Se$/Au-TAT nanoparticles could all produce ROS after X-ray irradiation, indicating that these nanoparticles could act as radiosensitizers for the purpose of radiotherapy. In order to further verify the radio-enhancement effect, a plate colony-formation experiment was conducted; 4T1 cells were co-culture with $Cu_{2-x}Se$, $Cu_{2-x}Se$/Au, and $Cu_{2-x}Se$/Au-TAT nanoparticles and were then irradiated at a dose of 0, 2, 4, and 6 Gy, respectively. As Figure 3D shows, with the increase in X-ray dose, the cell survival rate of each group showed a downward trend. However, there was a great diversity in the cell livability among different groups (Figure 3E). The survival rate S($Cu_{2-x}Se$/Au-TAT) < S($Cu_{2-x}Se$/Au) < S($Cu_{2-x}Se$) < S(control), and the calculated sensitization enhancement ratio (SER) values of $Cu_{2-x}Se$, $Cu_{2-x}Se$/Au, and $Cu_{2-x}Se$/Au-TAT were 1.76, 2.13, and 2.55, respectively. The cell livability of $Cu_{2-x}Se$/Au nanoparticles was lower than that of $Cu_{2-x}Se$ nanoparticles, indicating the radio-enhancement effect by combining $Cu_{2-x}Se$ and Au. $Cu_{2-x}Se$/Au-TAT nanoparticles had a higher therapeutic effect than $Cu_{2-x}Se$/Au nanoparticles, perhaps owing to the higher cellular uptake caused by TAT.

2.5. PTT/RT Combination Therapy In Vitro

The above results have proven that $Cu_{2-x}Se$/Au-TAT nanoparticles exerted the potential of not only killing tumor cells as a radiosensitizer, but also ablating tumor cells as a photothermal agent. As monotherapy of RT or PTT is not effective in eradicating tumors [42,43], the combination strategy of RT and PTT is a more desirable tool to enhance the treatment efficacy. Thus, we further studied the combined RT/PTT antitumor effect of $Cu_{2-x}Se$/Au-TAT nanoparticles in vitro.

ROS generation was tested by utilizing the probe of DCFH-DA. As demonstrated in Figure 4A, obvious higher green fluorescence intensity was found in the groups of $Cu_{2-x}Se$/Au-TAT or $Cu_{2-x}Se$/Au treated with X-ray and/or NIR, compared with other groups, indicating the potential of $Cu_{2-x}Se$/Au as an effective radiosensitizer to raise RT efficacy. The intensity of green fluorescence in the set treated with $Cu_{2-x}Se$/Au-TAT under X-ray and NIR was evidently higher than the group treated with $Cu_{2-x}Se$/Au-TAT under only X-ray, which may be attributed to the hyperthermia-induced cellular overactive state. When compared with the group treated with $Cu_{2-x}Se$/Au followed by NIR and X-ray, the fluorescence intensity of the group treated with $Cu_{2-x}Se$/Au-TAT followed by NIR and X-ray was slightly higher, which may be due to the improvement of cellular uptake by TAT.

Furthermore, DNA damage evaluation was conducted by γ-H_2AX foci detection through confocal microscopy. As can be seen from Figure 4B, the group of $Cu_{2-x}Se$/Au-TAT + PTT + RT showed the highest γ-H_2AX fluorescent spots, which was obviously higher than the group of $Cu_{2-x}Se$/Au-TAT+RT. The results of DNA damage were consistent with those of ROS generation detection, which further confirms that all three variables including RT, PTT, and TAT could promote ROS generation, thus resulting in DNA damage in the nucleus.

A cell colony formation assay, which is considered as the "gold standard" for assessment of cancer cells' response to X-ray irradiation, was also carried out [15]. The results of clonogenic assay and clonogenic survival assay are shown in Figure 4C,D. The cell

survival fraction reduced to 50% upon the treatment of $Cu_{2-x}Se$/Au-TAT + PTT, 29% of $Cu_{2-x}Se$/Au-TAT + RT, and 4% of $Cu_{2-x}Se$/Au-TAT + PTT + RT, indicating that combining PTT and RT had the best therapeutic effect. In addition to the radiosensitization and photothermal influence of $Cu_{2-x}Se$/Au, the presence of TAT led to the raised cellular uptake of nanoparticles and enhancement of the therapeutic effect.

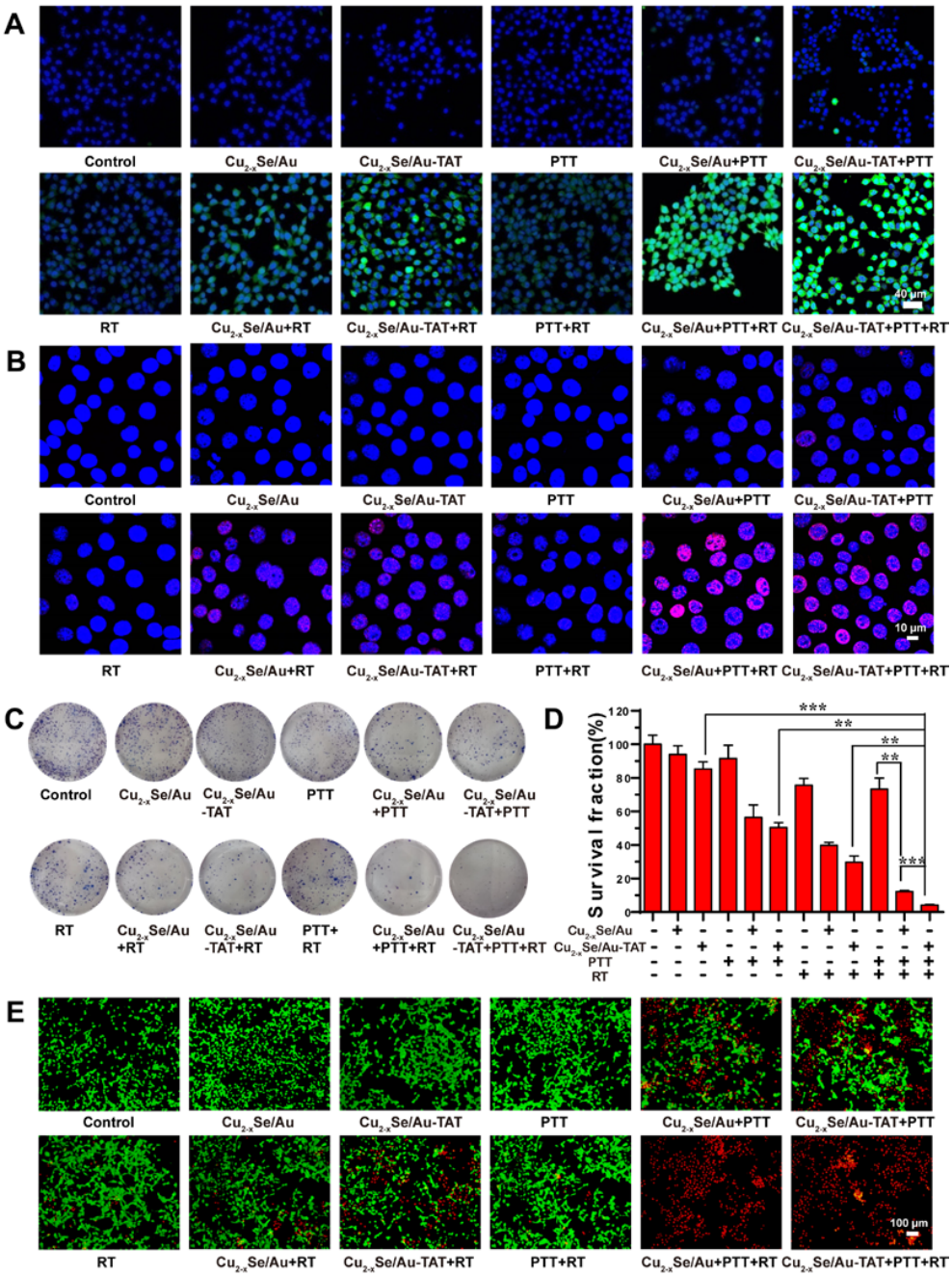

Figure 4. RT/PTT combination therapeutic efficacy *in vitro*. 4T1 cells underwent a 10-min irradiation with or without 808 nm light at 1.5 W/cm^2 and/or 4 Gy X-ray in control (PBS), $Cu_{2-x}Se$/Au, and $Cu_{2-x}Se$/Au-TAT nanoparticles. (**A**) Confocal fluorescence photos of DCF on 4T1 cells; (**B**) Confocal fluorescence images of DNA damage; (**C**) Clonogenic assay; (**D**) Clonogenic survival assay; (**E**) Fluorescence images of live–dead assay. *p* values were computed by the Student's *t*-test: ** $p < 0.01$, *** $p < 0.001$.

The PTT/RT combination therapy efficacy of $Cu_{2-x}Se$/Au-TAT nanoparticles was ulteriorly visually identified by calcein-AM/PI double staining. After receiving various

treatments, 4T1 cells presented different intensities of green (referring to live cells) and red (referring to dead cells) fluorescence. As can been seen from Figure 4E, barely no dead cells were found in the control, $Cu_{2-x}Se$/Au, and $Cu_{2-x}Se$/Au-TAT groups without any treatment, or NIR/X-ray-irradiated control groups, while more dead cells were seen in the $Cu_{2-x}Se$/Au and $Cu_{2-x}Se$/Au-TAT groups treated with NIR or X-ray. Notably, almost all tumor cells were dead in $Cu_{2-x}Se$/Au and $Cu_{2-x}Se$/Au-TAT treated with NIR and X-ray, clearly indicating the $Cu_{2-x}Se$/Au-TAT-induced combined PTT and RT effects.

2.6. PTT/RT Combination Efficacy of $Cu_{2-x}Se$/Au-TAT In Vivo

The photothermal performance of $Cu_{2-x}Se$/Au-TAT nanoparticles in vivo was investigated by irradiating the tumor areas of 4T1 tumor mice using an 808 nm laser after intratumoral injection of PBS and $Cu_{2-x}Se$/Au-TAT nanoparticles, and the temperature variation was recorded by an NIR camera. As illustrated in Figure 5A,B, after the tumors underwent a 10-min irradiation at 1.5 W/cm^2, the temperature of the tumor area with the treatment of $Cu_{2-x}Se$/Au-TAT nanoparticles rose to about 51.3 °C, while the group injected with PBS only increased to about 39.3 °C. The results show that $Cu_{2-x}Se$/Au-TAT nanoparticles had excellent photothermal efficacy in vivo.

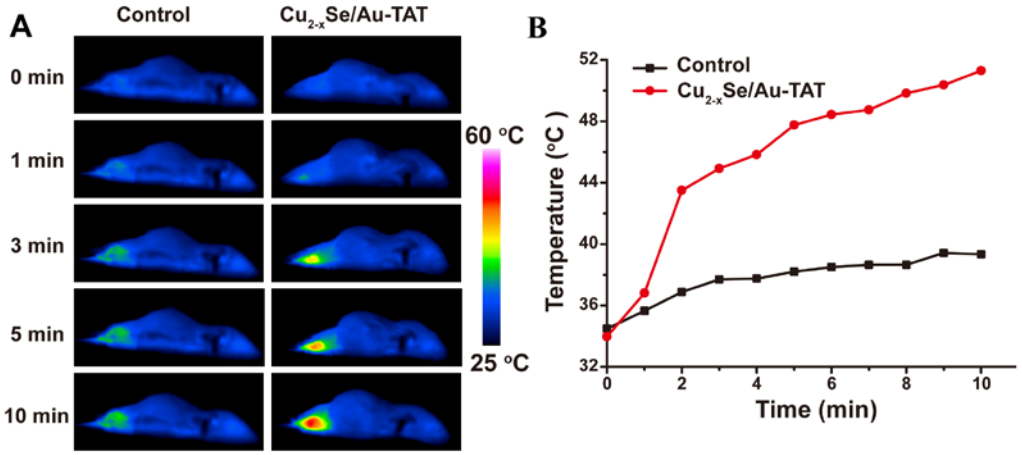

Figure 5. Photothermal effect and histology analysis in vivo. Typical IR images of the mice intratumorally injected with $Cu_{2-x}Se$/Au-TAT nanoparticles (**A**) and the change curve of temperature in tumor area (**B**) during a 10-min irradiation by 808 nm light at 1.5 W/cm^2.

Furthermore, the PTT and RT combination therapeutic effects of $Cu_{2-x}Se$/Au-TAT nanoparticles were explored in vivo. After all treatments, the mice were put to death and tumors were obtained (Figure 6A). The tumor volume curves are shown in Figure 6B,C. No significant differences could be detected in the groups of control, $Cu_{2-x}Se$/Au, $Cu_{2-x}Se$/Au-TAT, and control + PTT, except for a slight decrease in tumor in the control + RT group. Mice treated with $Cu_{2-x}Se$/Au-TAT + RT and $Cu_{2-x}Se$/Au-TAT + PTT had an inhibitory effect on tumor volume to 70.3% and 86.3%, respectively, when compared to the control group. Tumor volume from mice receiving $Cu_{2-x}Se$/Au or $Cu_{2-x}Se$/Au-TAT mediated PTT alone decreased rapidly in the early stage of treatment, but increased gradually in the later stage, demonstrating that PTT alone could not completely ablate the tumor. Meanwhile, when combining PTT and RT, the inhibitory effect of $Cu_{2-x}Se$/Au-TAT could reach 99.6%, indicating that combined PTT and RT could effectively achieve tumor ablation. Notably, the inhibitory effects of the $Cu_{2-x}Se$/Au-TAT-related groups were slightly better than those of the $Cu_{2-x}Se$/Au-related groups, which may be due to the better tissue permeability. To further estimate the therapeutic effect of $Cu_{2-x}Se$/Au-TAT-enhanced PTT/RT on tumors, tumor tissue sections were carried out by staining with hematoxylin and eosin (H&E) and antibodies against γ-H_2AX (Figure 6F,G). Compared with the control and the groups of $Cu_{2-x}Se$/Au and $Cu_{2-x}Se$/Au-TAT, obvious tumor nucleus fragmen-

tation and nuclear shrinkage were observed in the groups of $Cu_{2-x}Se$/Au-TAT + PTT and $Cu_{2-x}Se$/Au-TAT + RT, and this situation was further enhanced when receiving both PTT and RT. In the meantime, the group of $Cu_{2-x}Se$/Au-TAT + PTT + RT dramatically upregulated the expression levels of γ-H_2AX, indicating that serious DNA damage was induced by PTT/RT combined treatment.

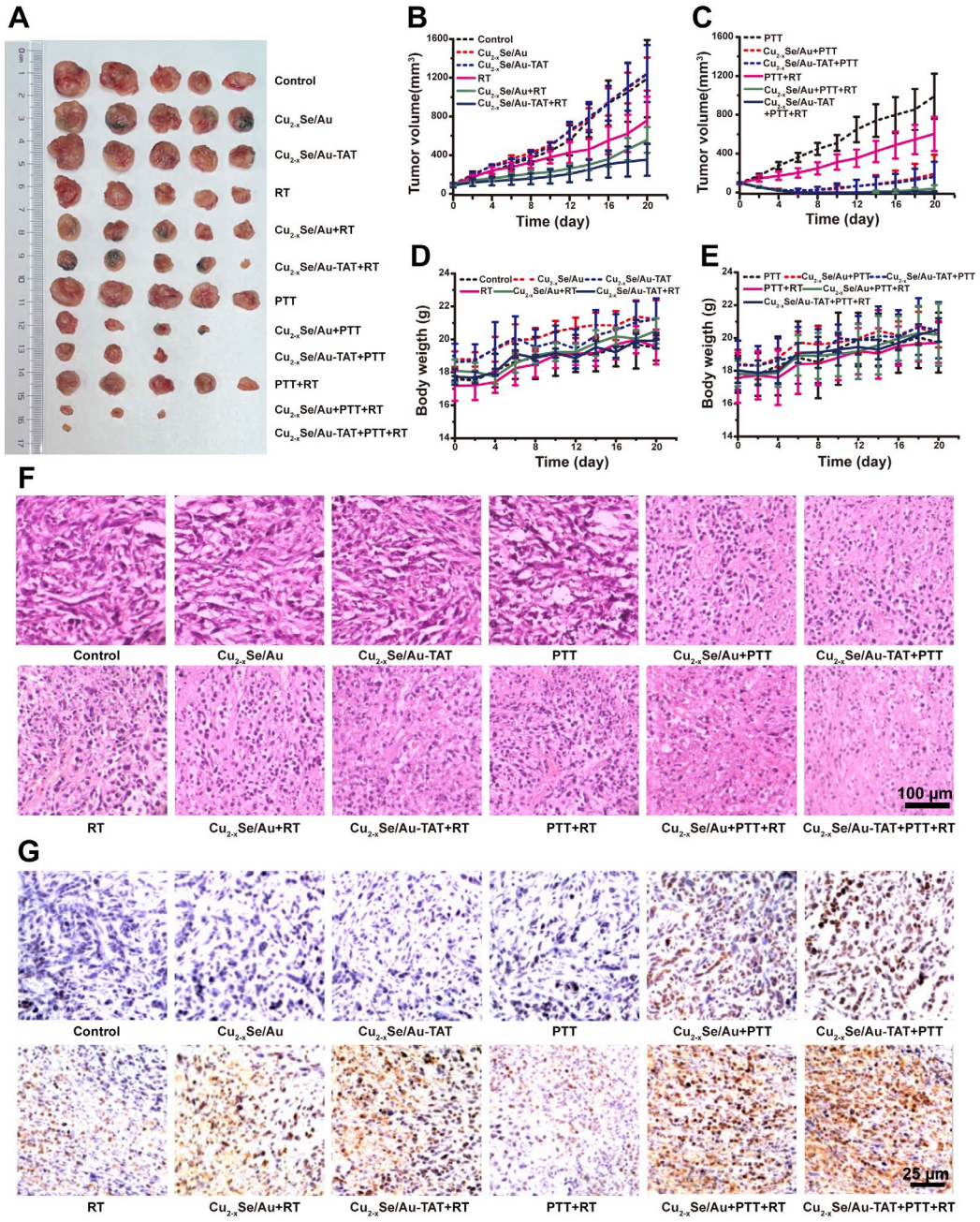

Figure 6. RT/PTT combination efficacy in vivo. (**A**) Photographs of tumors removed from mice under different treatments; (**B**,**C**) Tumor volume curves of mice under different treatments; (**D**,**E**) Body weight curves of 4T1 mice with multiple treatments. Photos of tumor specimen sections with (**F**) H&E and (**G**) γ-H_2AX staining.

In order to evaluate the potential by-effects of these nanomaterials and the curative treatments, the chief organs of the mice, which consisted of heart, liver, spleen, and kidney, were acquired for H&E staining. No significant tissue injury and adverse effects on the main organs of mice were observed (Figure S2). Simultaneously, no obvious abnormalities were

found in the body weight of the $Cu_{2-x}Se$/Au-TAT-treated mice (Figure 6D,E). These results indicate the high biocompatibility of $Cu_{2-x}Se$/Au-TAT nanoparticles within tested days.

3. Materials and Methods

3.1. Materials

$CuCl_2{\cdot}2H_2O$ was supplied by Kemiou Chemical Reagent (Tianjin, China). Sodium hydroxide (NaOH) was bought from Chemical Reagent Wholesale Company (Tianjin, China). $N_2H_4{\cdot}H_2O$ was furnished by Taimo Biological Technology Co., Ltd. (Tianjin, China). PVP K30 (MW = 40,000) was procured from Shengpei New Material Co., Ltd. (Shanghai, China). Selenium powder (Se, ~100 mesh, ≥99.5%) and sodium borohydride ($NaBH_4$) were supplied by CSI Biochemical Technology Co., Ltd. (Tianjin, China). $HAuCl_4$ was supplied by Fengchuan Chemical Reagent Co., Ltd. (Tianjin, China). TAT peptide was procured from China Peptides (99.8%, Shanghai, China). FITC and calcein-AM/PI double staining kit were bought from Meilun Biotechnology Co., Ltd. (Dalian, China). MTT, DCFH-DA, and 4′,6′-diamidino-2-phylindole (DAPI) were offered by Sigma-Aldrich (St. Louis, MO, USA). Hoechst 33258 was obtained from Invitrogen (Carlsbad, CA, USA). Giemsa stain was supplied by Tianjin Solomon Biotechnology Co., Ltd. (Tianjin, China). Monoclonal antibodies against γ-H_2AX were procured from Abcam (Cambridge, MA, USA). Alexa-Fluor488-labeled goat anti-rabbit secondary antibody was provided by Biyuntian Biological Reagent Co., Ltd. (Shanghai, China).

3.2. Cell Lines and Animals

4T1 and HUVECs were furnished by Biovector NTCC (Beijing, China). All cells were cultured with 10% FBS and 1% penicillin/streptomycin with 5% CO_2 at 37 °C. Female BALB/c mice (4–6 weeks old) were supplied by SPF Biotechnology Co., Ltd. (Beijing, China). The mouse breast cancer xenograft model was developed through 100 μL subcutaneous injection of sterile phosphate buffer saline (PBS) (including 1.0×10^6 4T1 cells) on the right back of each mouse. When the tumor volume reached ~100 mm^3, the mice could be used for the following in vivo experiments. All animal research was approved by the Animal Ethics Committee of Tianjin Medical University, and all procedures were carried out conforming with the Guide for the Care and Use of Laboratory Animals.

3.3. Synthesis of $Cu_{2-x}Se$ Nanoparticles, $Cu_{2-x}Se$/Au Nanoparticles, and $Cu_{2-x}Se$/Au-TAT Nanoparticles

Hollow $Cu_{2-x}Se$ nanoparticles were prepared in reference to former methods, with minor modifications [44]. Briefly, 0.1 mmol $CuCl_2{\cdot}2H_2O$ was directly dissolved in a mixture of 58 mL 2-propanol and 2 mL water, following the addition of 0.2 g PVP and 0.24 mmol of NaOH solution in 1.2 mL 2-propanol. Next, the solution was reacted for 20 min. After that, 0.2 mL $N_2H_4{\bullet}H_2O$ (35 wt%) was further added at a very slow speed, and the solution was stirred for another 10 min. Orange Cu_2O sediments were immediately apparent upon adding $N_2H_4{\bullet}H_2O$. The obtained Cu_2O nanoparticles were gained by centrifugation and subsequent water washing.

In the preparation of hollow $Cu_{2-x}Se$ nanoparticles, 0.1 mmol of Se power and 0.3 mmol of $NaBH_4$ were first dissolved in 20 mL water under the protection of N_2, and the mixed solution was stirred for 30 min to acquire the Se^{2-} solution. Then, the above-mentioned double portion of Cu_2O nanoparticles was added to the resultant Se^{2-} suspension and stirred for 3 h. The obtained $Cu_{2-x}Se$ nanoparticles were gained by centrifugation and subsequent water washing.

Next, 0.05 M of $HAuCl_4$ solution was placed into the $Cu_{2-x}Se$ nanoparticles dropwise with a mole ratio of 1:0.375 ($Cu_{2-x}Se$: $HAuCl_4$) to prepare the $Cu_{2-x}Se$/Au nanoparticles. The synthetic products were gained by centrifugation and redispersed in water.

To synthesize $Cu_{2-x}Se$/Au-TAT nanoparticles, TAT solution was added to the above synthesized $Cu_{2-x}Se$/Au solution dropwise refering to a mass ratio of $Cu_{2-x}Se$/Au:TAT of 1:1.5, followed by stirring the mixture for 1 h. Finally, $Cu_{2-x}Se$/Au-TAT nanoparticles were gained by centrifugation and subsequent water washing.

3.4. Characterization

The morphological features of the obtained samples were observed through a HT7700 TEM (Hitachi, Tokyo, Japan). The elemental mapping was recorded by a JEM-2100F instrument (JEOL, Tokyo, Japan). The absorbance of UV-vis-NIR was obtained by employing a UV-1510 spectrophotometer (Thermo Fisher Scientific, Waltham, MA, USA). The fluorescence spectrum was acquired by an F-7000 fluorescence spectrophotometer (Hitachi, Tokyo, Japan). The hydrodynamic size (Dh) and zeta potentials of the samples were obtained by a ZS90 Zetasizer (Malvern, Malvern, UK) (at $Cu_{2-x}Se$ concentration of 40 μg/mL. XPS was employed to study the valence states of elementary substances by utilizing an ESCALab 250XiSigma Probe instrument (Thermo Fisher Scientific, Waltham, MA, USA). Cu and Au content of the nanoparticles were determined by a Thermo Electron Corporation X7 ICP-OES (Thermo Fisher Scientific, Waltham, MA, USA). A Rad Source RS-2000 Pro (Rad Source Technologies, Atlanta, GA, USA) was performed for radiation.

3.5. Photothermal Experiments

To estimate the photothermal performance of $Cu_{2-x}Se$/Au-TAT nanoparticles, the aqueous suspensions of nanoparticles with multiple concentrations (0, 20, 40, 80, 120, 160 μg/mL) underwent irradiation with 808 nm light (1.0 W/cm^2, 10 min). In addition, $Cu_{2-x}Se$/Au-TAT nanoparticles (80 μg/mL) underwent irradiation for 10 min at various light powers (0.5, 1.0, and 1.5 W/cm^2). The photothermal stability of $Cu_{2-x}Se$/Au-TAT nanoparticles (80 μg/mL) was examined by laser ON/OFF assays for 5 cycles. For each cycle, the $Cu_{2-x}Se$/Au-TAT aqueous solution underwent irradiation for 10 min with 808 nm light (1.0 W/cm^2), following by light shut off to allow the solution to cool down to ambient temperature. The temperatures of the samples were recorded by an FLIR infrared camera (Nashua, NH, USA).

The photothermal conversion efficiency (η) of $Cu_{2-x}Se$/Au-TAT was calculated according to the following equations:

$$\eta = \frac{hs(T_{max} - T_{sur}) - Q_{dis}}{I(1 - 10^{-A})} \quad (1)$$

$$hs = \frac{mc}{\tau} = \frac{mcLn(\theta)}{-t} \quad (2)$$

$$\theta = \frac{(T - T_{sur})}{(T_{max} - T_{sur})} \quad (3)$$

where h is the heat transfer coefficient, s is the surface area of the container, Tmax is the maximum temperature of the $Cu_{2-x}Se$/Au-TAT solution, Tsur is the maximum temperature of the surroundings, Qdis is the quantity of heat generated when the reagent is water, I is the laser power, A is the absorbance of the $Cu_{2-x}Se$/Au-TAT solution at 808 nm, m is the mass of the water solution of nanoparticles, c is the specific heat capacity of the water (4.2 J/g), τ is the time constant of the sample, and T and t are the temperature of the sample and the time of the sample during the cooling process, respectively.

3.6. Detection of ROS

ROS detection was carried out by employing DCFH-DA as the probe. Firstly, 20 μL of DMSO solution containing DCFH-DA (0.02 M) and 2 mL of sodium hydroxide (0.01 M) were reacted in the absence of light at ambient temperature for 30 min. Afterwards, 18 mL of phosphate buffer (pH 7.2) was added into the above solution to stop the reaction. Next, DCFH was added into the sample solutions of all the groups. Eight groups were set: Control, $Cu_{2-x}Se$, $Cu_{2-x}Se$/Au, $Cu_{2-x}Se$/Au-TAT, Control + X-ray, $Cu_{2-x}Se$ + X-ray, $Cu_{2-x}Se$/Au + X-ray, $Cu_{2-x}Se$/Au-TAT + X-ray. The final concentrations of DCFH were set at 10 μM, the final concentrations of $Cu_{2-x}Se$ were set at 40 μg/mL, and X-ray was administered at 4 Gy. Afterwards, solutions were shaken on the shaker for 2 h. Finally,

the fluorescence of the solutions was obtained using an F-7000 spectrofluorometer with an excited wavelength of 488 nm.

3.7. Cellular Uptake Experiment

Firstly, $Cu_{2-x}Se$/Au-TAT or $Cu_{2-x}Se$/Au was labelled with FITC by adding FITC (100 μg/mL) into $Cu_{2-x}Se$/Au-TAT or $Cu_{2-x}Se$/Au (1 mg/mL) and reacted for 24 h. The exceeded FITC was removed through washing with water. Next, 4T1 cells were planted into 12-well plates (1×10^5 per well) and cultured at 37 °C for 24 h. Subsequently, 4T1 cells were incubated with the medium containing free FITC, FITC-labeled $Cu_{2-x}Se$/Au-TAT nanoparticles, and $Cu_{2-x}Se$/Au nanoparticles for 4 h. After cleaning three times with PBS, the cells were fastened for 10 min, employing 4% paraformaldehyde. Finally, the cell nucleus was stained by DAPI and imaged, employing confocal fluorescence microscopy.

3.8. In Vitro Cytotoxicity Study

The cell cytotoxicity of $Cu_{2-x}Se$/Au-TAT nanoparticles towards 4T1 cells and HUVECs was evaluated using the MTT method. Cells were spread evenly in 96-well plates (5×10^3 per well) and cultured for twenty-four hours. Then, cells were cocultured with the medium containing $Cu_{2-x}Se$/Au-TAT nanoparticles (10, 20, 40, 60, 80, and 120 μg/mL, respectively). After 4-h incubation, the cells were cleaned twice, employing PBS, 100 μL of fresh culture was added, and they were then continuously incubated for 20 h. Subsequently, the above cells were incubated for 4 h absent from dark. The medium was then discarded and they continued to be incubated with 100 μL of 1 mg/mL MTT solution. Afterwards, each well of the medium was discarded, 150 μL of DMSO was further added, and the plates then underwent a 5-min shake. The absorbance of each well was detected at 490 nm, employing a microplate reader.

To evaluate the photothermal ablation effects towards cancer cells, cells were planted into 96-well plates (5×10^3 per well) at 37 °C overnight and incubated with multiple concentrations of $Cu_{2-x}Se$/Au-TAT nanoparticles (30, 40, 50, 60, 70, and 80 μg/mL), respectively. After 4 h, the cells underwent irradiation with 808 nm light at 1.0 or 1.5 W/cm^2 for 10 min, were washed two times, employing PBS, and supplemented with 100 μL of fresh DMEM for another 20 h. The cell livability was performed via the standard MTT test.

3.9. In Vitro Clonogenic Assay

4T1 cells were spread evenly into 6-well plates with different densities (250, 500, 1000, and 2000 per well) and cultured for 24 h. Next, the culture containing $Cu_{2-x}Se$, $Cu_{2-x}Se$/Au, and $Cu_{2-x}Se$/Au-TAT nanoparticles at $Cu_{2-x}Se$ concentration of 40 μg/mL was added and incubated for 4 h, and then underwent irradiation with X-ray at 0, 2, 4, and 6 Gy, respectively. After washing with PBS and refreshing medium, all the treated groups were further incubated for 7 d. Finally, the above cells were rinsed two times with PBS, underwent 15-min immobilization with methanol, and were further stained using Giemsa dye for 30 min. Colonies covering at least 50 cells were counted, and the survival fraction (SF) was computed by (surviving colonies)/(cells seeded × plating efficiency) to evaluate the effects of different treatments.

SER was defined with the following formulae:

$$S = 1 - (1 - \exp(-D/D_0))^N \quad (4)$$

where S represents the cell survival fraction at a certain X-ray dose, D is representative of the dose of the irradiated X-ray, D_0 acts as the average lethal dose of radiation representing the sensitivity of cells to X-ray, and N represents the cell's self-healing ability. D_0 and N were acquired by SPSS. SER was calculated as follows:

$$SER = D_q \text{ (control group)}/D_q \text{ (treated group)} \quad (5)$$

$$D_q = \text{In(N)} \times D_0 \quad (6)$$

where D_q is representative of the quasi-threshold dose, which represents the ability to repair sublethal injury.

In the combination therapy experiment, 4T1 cell were inoculated into 96-well plates (3000 cells/well). The experiment was divided into 12 groups: (1) Control (PBS), (2) $Cu_{2-x}Se$/Au, (3) $Cu_{2-x}Se$/Au-TAT, (4) Control + PTT, (5) $Cu_{2-x}Se$/Au + PTT, (6) $Cu_{2-x}Se$/Au-TAT + PTT, (7) Control + RT, (8) $Cu_{2-x}Se$/Au + RT, (9) $Cu_{2-x}Se$/Au-TAT + RT, (10) Control + PTT + RT, (11) $Cu_{2-x}Se$/Au + PTT + RT, (12) $Cu_{2-x}Se$/Au-TAT + PTT + RT. After 4 h incubation, groups 4, 5, 6, 10, 11, and 12 underwent 10-min irradiation with 808 nm light at 1.5 W/cm^2. Afterwards, groups 7, 8, 9, 10, 11, and 12 were exposed to X-ray at 4 Gy. The above cells with different treatments were then rinsed with PBS, trypsinized, and seeded into 6-well plates for incubation of 7 d. Finally, the cells were rinsed with PBS, underwent 15-min immobilization with methanol, were further stained using Giemsa dye for 30 min, and counted.

3.10. In Vitro Detection of ROS Generation

4T1 cells were inoculated on confocal dishes (8×10^4 per well). Twelve groups were set as described previously. Firstly, cells were incubated with control, $Cu_{2-x}Se$/Au, and $Cu_{2-x}Se$/Au-TAT nanoparticles at a $Cu_{2-x}Se$ concentration of 40 μg/mL for 4 h. Cells were then washed three times with PBS and underwent a 20-min incubation with DCFH-DA (10 μM) and Hoechst 33,258 (10 μM) at 37 °C. After being washed three times with PBS and adding 1 mL of PBS, the experimental groups were treated with or without a 10-min NIR irradiation (808 nm, 1.5 W/cm^2), followed by treatment with or without X-ray (4 Gy), respectively. Finally, a fluorescence microscope was employed to observe the ROS created within cells

3.11. In Vitro DNA Damage Evaluation

To assess DNA double-strand injury, 4T1 cells in logarithmic growth were spread evenly into 12-well plates (8×10^4 per well) and cultured for 24 h. Groups were set the same as in the in vitro ROS detection tests. These cells were incubated with control, $Cu_{2-x}Se$/Au, and $Cu_{2-x}Se$/Au-TAT nanoparticles at a $Cu_{2-x}Se$ concentration of 40 μg/mL for 4 h, and then treatments were performed with or without a 10-min NIR irradiation (808 nm, 1.5 W/cm^2) and/or X-ray (4 Gy). Afterwards, these cells were washed three times with PBS, and then fastened for 10 min by 4% paraformaldehyde. Afterwards, the cells underwent a 10-min permeation by 0.2% Triton X-100 and a 1-h blocking with 3% BSA. After that, the cells were incubated with anti-γ-H_2AX monoclonal antibody (1:250) at 4 °C overnight, followed by a treatment of secondary Alexa-488-conjugated goat anti-rabbit antibody (1:300). Finally, the cell nuclei underwent a 10-min staining by DAPI (1:900) and were imaged, employing confocal fluorescence microscopy.

3.12. Live–Dead Cell-Staining Assay

4T1 cells were inoculated in 12-well plates (1×10^5 per well) and incubated for 24 h. Then, these cells were incubated with control, $Cu_{2-x}Se$/Au, and $Cu_{2-x}Se$/Au-TAT nanoparticles at a $Cu_{2-x}Se$ concentration of 60 μg/mL for 4 h. Following the various treatments mentioned above, a calcein-AM/PI double staining kit was employed to stain for 30 min to make a distinction between the live cells (green) and the dead cells (red). Finally, a Zeiss fluorescence microscope (Jena, Germany) was employed to observe the acquired results.

3.13. In Vivo Antitumor Efficacy

The 4T1 tumor-bearing mice were distributed into twelve groups of 6 at random, as described above, as long as the tumor grew to 100 mm^3. The twelve groups of mice were then intratumorally injected with 50 μL control, $Cu_{2-x}Se$/Au (at a $Cu_{2-x}Se$ concentration of 4 mg/mL), and $Cu_{2-x}Se$/Au-TAT nanoparticles (at a $Cu_{2-x}Se$ concentration of 4 mg/mL), respectively. The mice of different groups then underwent irradiation with

or without a 10-min NIR light (808 nm, 1.5 W/cm^2) and/or X-ray (6Gy). The volume of tumors and the mouse weight was noted every second day during the whole treatment period. The volume of tumors was measured referring to the following computing formula: volume = 1/2(width^2 × length). All tumors were imaged on the 20th day after treatments.

3.14. Histology Analysis In Vivo

The chief organs, which consisted of heart, liver, spleen, and kidney, were acquired for histology analysis after various treatments. These removed organs were fastened with 4% paraformaldehyde and were further made into paraffin sections for H&E staining. Additionally, the tumors were obtained after treatments for 48 h, fastened by 4% paraformaldehyde, and further embedded in paraffin. Slices were stained by H&E and γ-H2AX antibody. All these images of tissue slices were imaged, employing a fluorescence microscope.

3.15. Statistical Analysis

All the above results were assessed via Student's *t*-test or one-way ANOVA. The experimental results were given as mean ± standard deviation (SD). $p < 0.05$ was representative of statistical significance.

4. Conclusions

In conclusion, multifunctional $Cu_{2-x}Se$/Au-TAT nanoparticles were prepared by a spontaneous redox process between hollow $Cu_{2-x}Se$ nanoparticles and $HAuCl_4$, with subsequent surface modification with TAT. They exhibited excellent stability, enhanced tumor cell uptake, excellent radiosensitization, and outstanding photothermal properties. Both in vitro and in vivo, compared with PTT or RT monotherapy, combination therapy of PTT and RT achieved a significant combined anticancer effect. This study provided an efficient mentality for RT/PTT combination therapy against breast cancer.

Supplementary Materials: The following supporting information can be downloaded at: https://www.mdpi.com/article/10.3390/molecules28010423/s1, Figure S1: XPS survey spectra of (A) $Cu_{2-x}Se$/Au nanoparticles and (B) $Cu_{2-x}Se$nanoparticles; (C) Cu and (D) Se spectra of $Cu_{2-x}Se$ nanoparticles. Figure S2: H&E staining images of tissue sections from the mice after different treatments.

Author Contributions: Conceptualization, R.R., Y.W. and X.Y.; methodology, S.G. and R.R.; validation, R.R., S.G., X.J. and Z.Q.; investigation, R.R. and S.G.; resources, S.G. and Z.G.; writing—original draft preparation, R.R.; writing—review and editing, X.Y., Y.W. and M.C.; supervision, M.C.; project administration, X.Y.; funding acquisition, R.R. All authors have read and agreed to the published version of the manuscript.

Funding: This research was funded by the Science & Technology Development Fund of Tianjin Education Commission for Higher Education, grant number 2021KJ257.

Institutional Review Board Statement: The animal study protocol was approved by the university animal care and use committee of Tianjin Medical University.

Informed Consent Statement: Not applicable.

Data Availability Statement: Written informed consent has been obtained from the patient(s) to publish this paper.

Conflicts of Interest: The authors declare no conflict of interest.

Sample Availability: Not applicable.

References

1. Xie, J.; Gong, L.; Zhu, S.; Yong, Y.; Gu, Z.; Zhao, Y. Emerging Strategies of Nanomaterial-Mediated Tumor Radiosensitization. *Adv. Mater.* **2018**, *31*, 1802244. [CrossRef]
2. Song, G.; Cheng, L.; Chao, Y.; Yang, K.; Liu, Z. Emerging Nanotechnology and Advanced Materials for Cancer Radiation Therapy. *Adv. Mater.* **2017**, *29*, 1700996. [CrossRef]
3. Wang, H.; Mu, X.; He, H.; Zhang, X.-D. Cancer Radiosensitizers. *Trends Pharmacol. Sci.* **2018**, *39*, 24–48. [CrossRef]

4. Her, S.; Jaffray, D.A.; Allen, C. Gold Nanoparticles for Applications in Cancer Radiotherapy: Mechanisms and Recent Advancements. *Adv. Drug Delivery Rev.* **2017**, *109*, 84–101. [CrossRef]
5. Deng, Y.; Tian, X.; Lu, S.; Xie, M.; Hu, H.; Zhang, R.; Lv, F.; Cheng, L.; Gu, H.; Zhao, Y.; et al. Fabrication of Multifoliate PtRu Bimetallic Nanocomplexes for Computed Tomography Imaging and Enhanced Synergistic Thermoradiotherapy. *ACS Appl. Mater. Interfaces* **2018**, *10*, 31106–31113. [CrossRef]
6. Ma, N.; Liu, P.; He, N.; Gu, N.; Wu, F.-G.; Chen, Z. Action of Gold Nanospikes-Based Nanoradiosensitizers: Cellular Internalization, Radiotherapy, and Autophagy. *ACS Appl. Mater. Interfaces* **2017**, *9*, 31526–31542. [CrossRef]
7. Li, X.; Yu, L.; Zhang, C.; Niu, X.; Sun, M.; Yan, Z.; Wang, W.; Yuan, Z. Tumor acid microenvironment-activated self-targeting & splitting gold nanoassembly for tumor chemo-radiotherapy. *Bioact. Mater.* **2022**, *7*, 377–388.
8. Ni, K.; Lan, G.; Veroneau, S.S.; Duan, X.; Song, Y.; Lin, W. Nanoscale Metal-Organic Frameworks for Mitochondria-Targeted Radiotherapy-Radiodynamic Therapy. *Nat. Commun.* **2018**, *9*, 4321–4333. [CrossRef]
9. Lu, K.; He, C.; Guo, N.; Chan, C.; Ni, K.; Lan, G.; Tang, H.; Pelizzari, C.; Fu, Y.-X.; Spotto, M.T.; et al. Low-Dose X-ray Radiotherapy–Radiodynamic Therapy via Nanoscale Metal–Organic Frameworks Enhances Checkpoint Blockade Immunotherapy. *Nat. Biomed. Eng.* **2018**, *2*, 600–610. [CrossRef]
10. Liu, H.; Cheng, R.; Dong, X.; Zhu, S.; Zhou, R.; Yan, L.; Zhang, C.; Wang, Q.; Gu, Z.; Zhao, Y. BiO_{2-x} Nanosheets as Radiosensitizers with Catalase-Like Activity for Hypoxia Alleviation and Enhancement of the Radiotherapy of Tumors. *Inorg. Chem.* **2020**, *59*, 3482–3493. [CrossRef]
11. Wang, X.; Guo, Z.; Zhang, C.; Zhu, S.; Li, L.; Gu, Z.; Zhao, Y. Ultrasmall BiOI Quantum Dots with Efficient Renal Clearance for Enhanced Radiotherapy of Cancer. *Adv. Sci* **2020**, *7*, 1902561. [CrossRef] [PubMed]
12. Yang, R.; Wang, P.; Lou, K.; Dang, Y.; Tian, H.; Li, Y.; Gao, Y.; Huang, W.; Zhang, Y.; Liu, X.; et al. Biodegradable Nanoprobe for NIR-II Fluorescence Image-Guided Surgery and Enhanced Breast Cancer Radiotherapy Efficacy. *Adv. Sci.* **2022**, *9*, 2104728. [CrossRef] [PubMed]
13. Song, G.; Liang, C.; Yi, X.; Zhao, Q.; Cheng, L.; Yang, K.; Liu, Z. Perfluorocarbon-Loaded Hollow Bi_2Se_3 Nanoparticles for Timely Supply of Oxygen under Near-Infrared Light to Enhance the Radiotherapy of Cancer. *Adv. Mater.* **2016**, *28*, 2716–2723. [CrossRef] [PubMed]
14. Yong, Y.; Cheng, X.; Bao, T.; Zu, M.; Yan, L.; Yin, W.; Ge, G.; Wang, D.; Gu, Z.; Zhao, Y. Tungsten Sulfide Quantum Dots as Multifunctional Nanotheranostics for in Vivo Dual-Modal Imaging-Guided Photothermal/Radiotherapy Synergistic Therapy. *ACS Nano* **2015**, *9*, 12451–12463. [CrossRef]
15. Gao, F.; Wang, D.; Zhang, B.; Ghosal, A.; Guo, Z.; Miao, Y.; Li, G.; Liu, X.; Lu, J.; Yu, J.; et al. Facile Synthesis of Bi_2S_3-MoS_2 Heterogeneous Nanoagent as Dual Functional Radiosensitizer for Triple Negative Breast Cancer Theranostics. *Chem. Eng. J.* **2020**, *395*, 125032. [CrossRef]
16. Huang, Q.; Zhang, S.; Zhang, H.; Han, Y.; Liu, H.; Ren, F.; Sun, Q.; Li, Z.; Gao, M. Boosting the Radiosensitizing and Photothermal Performance of $Cu_{2-x}Se$ Nanocrystals for Synergetic Radiophotothermal Therapy of Orthotopic Breast Cancer. *ACS Nano* **2019**, *13*, 1342–1353. [CrossRef]
17. Datta, N.R.; Puric, E.; Klingbiel, D.; Gomez, S.; Bodis, S. Hyperthermia and Radiation Therapy in Locoregional Recurrent Breast Cancers: A Systematic Review and Meta Analysis. *Int. J. Radiat. Oncol. Biol. Phys.* **2016**, *94*, 1073–1087. [CrossRef]
18. Datt, N.R.; Ordóñez, S.G.; Gaipl, U.S.; Paulides, M.M.; Crezee, H.; Gellermann, J.; Marder, D.; Puric, E.; Bodis, S. Local Hyperthermia Combined With Radiotherapy and-/or Chemotherapy: Recent Advances And Promises For The Future. *Cancer Treat. Rev.* **2015**, *41*, 742–753. [CrossRef]
19. Melancon, M.P.; Lu, W.; Zhong, M.; Zhou, M.; Liang, G.; Elliott, A.M.; Hazle, J.D.; Myers, J.N.; Li, C.; Jason Stafford, R. Targeted Multifunctional Gold-Based Nanoshells for Magnetic Resonance-Guided Laser Ablation of Head and Neck Cancer. *Biomaterials* **2011**, *32*, 7600–7608. [CrossRef]
20. Sahu, A.; Kwon, I.; Tae, G. Improving Cancer Therapy Through the Nanomaterials-Assisted Alleviation of Hypoxia. *Biomaterials* **2020**, *228*, 119578. [CrossRef]
21. Kampinga, H.H. Cell Biological Effects of Hyperthermia Alone or Combined with Radiation or Drugs: A Short Introduction to Newcomers in the Field. *Int. J. Hyperthermia* **2006**, *22*, 191–196. [CrossRef] [PubMed]
22. Genet, S.C.; Fujii, Y.; Maeda, J.; Kaneko, M.; Genet, M.D.; Miyagawa, K.; Kato, T.A. Hyperthermia inhibits homologous recombination repair and sensitizes cells to ionizing radiation in a time- and temperature-dependent manner. *J. Cell. Physiol.* **2013**, *228*, 1473–1481. [CrossRef] [PubMed]
23. Hu, P.; Hou, X.; Yu, X.; Wei, X.; Li, Y.; Yang, D.; Jiang, X. Folic Acid-Conjugated Gold Nanostars for Computed Tomography Imaging and Photothermal/Radiation Combined Therapy. *ACS Appl. Bio Mater.* **2021**, *4*, 4862–4871. [CrossRef] [PubMed]
24. Wang, T.; Zhang, H.; Liu, H.; Yuan, Q.; Ren, F.; Han, Y.; Sun, Q.; Li, Z.; Gao, M. Boosting H_2O_2-Guided Chemodynamic Therapy of Cancer by Enhancing Reaction Kinetics Through Versatile Biomimetic Fenton Nanocatalysts and the Second Near-infrared Light Irradiation. *Adv. Funct. Mater.* **2020**, *30*, 1906128. [CrossRef]
25. Zhang, H.; Wang, T.; Liu, H.; Ren, F.; Qiu, W.; Sun, Q.; Yan, F.; Zheng, H.; Li, Z.; Gao, M. Second Near-Infrared Photodynamic Therapy and Chemotherapy of Orthotopic Malignant Glioblastoma with Ultra-Small $Cu_{2-x}Se$ Nanoparticles. *Nanoscale* **2019**, *11*, 7600–7608. [CrossRef]

26. Wang, Y.; Li, Z.; Hu, Y.; Liu, J.; Guo, M.; Wei, H.; Zheng, S.; Jiang, T.; Sun, X.; Ma, Z.; et al. Photothermal Conversion-Coordinated Fenton-like and Photocatalytic Reactions of $Cu_{2-x}Se$-Au Janus Nanoparticles for Tri-Combination Antitumor Therapy. *Biomaterials* **2020**, *255*, 120167. [CrossRef]
27. Rayman, M.P. Selenium in cancer prevention: A review of the evidence and mechanism of action. *Proc. Nutr. Soc.* **2005**, *64*, 527–542. [CrossRef]
28. Uriu-Adams, J.Y.; Keen, C.L. Copper, oxidative stress, and human health. *Mol. Aspects. Med.* **2005**, *26*, 268–298. [CrossRef]
29. Verma, A.; Stellacci, F. Effect of Surface Properties on Nanoparticle-Cell Interaction. *Small* **2010**, *6*, 12–21. [CrossRef]
30. Yuan, H.; Fales, A.M.; Vo-Dinh, T. TAT Peptide-Functionalized Gold Nanostars: Enhanced Intracellular Delivery and Effient NIR Photothermal Therapy Using Ultralow Irradiance. *J. Am. Chem. Soc.* **2012**, *134*, 11358–11361. [CrossRef]
31. Zhang, D.; Wang, J.; Xu, D. Cell-Penetrating Peptides as Noninvasive Transmembrane Vectors for The Development of Novel Multifunctional Drug-Delivery Systems. *J. Control. Release* **2016**, *229*, 130–139. [CrossRef]
32. Wan, G.; Cheng, Y.; Song, J.; Chen, Q.; Chen, B.; Liu, Y.; Ji, S.; Chen, H.; Wang, Y. Nucleus-Targeting Near-Infrared Nanoparticles Based on TAT Peptide Conjugated IR780 for Photo-Chemotherapy of Breast Cancer. *Chem. Eng. J.* **2020**, *380*, 122458–122474. [CrossRef]
33. Wang, D.; Dong, H.; Li, M.; Cao, Y.; Yang, F.; Zhang, K.; Dai, W.; Wang, C.; Zhang, X. Erythrocyte–Cancer Hybrid Membrane Camouflaged Hollow Copper Sulfide Nanoparticles for Prolonged Circulation Life and Homotypic-Targeting Photothermal/Chemotherapy of Melenoma. *ACS Nano* **2018**, *12*, 5241–5252. [CrossRef] [PubMed]
34. Li, Q.; Sun, L.; Hou, M.; Chen, Q.; Yang, R.; Zhang, L.; Xu, Z.; Kang, Y.; Xue, P. Phase-Change Material Packaged within Hollow Copper Sulfide Nanoparticles Carrying Doxorubicin and Chlorin e6 for Fluorescence-Guided Trimodal Therapy of Cancer. *ACS Appl. Mater. Interfaces* **2019**, *11*, 417–429. [CrossRef]
35. Xue, X.; Liu, H.; Wang, S.; Hu, Y.; Huang, B.; Li, M.; Gao, J.; Wang, X.; Su, J. Neutrophil-erythrocyte hybrid membrane-coated hollow copper sulfide nanoparticles for targeted and photothermal/ anti-inflammatory therapy of osteoarthritis. *Compos. Part B Eng.* **2022**, *237*, 109855. [CrossRef]
36. Yang, Y.; Zhu, W.; Dong, Z.; Chao, Y.; Xu, L.; Chen, M.; Liu, Z. 1D Coordination Polymer Nanofibers for Low-Temperature Photothermal Therapy. *Adv. Mater.* **2017**, *29*, 1703588. [CrossRef]
37. Zhang, Y.; Zhu, C.; Zhang, Z.; Zhao, J.; Yuan, Y.; Wang, S. Oxidation Triggerd Formation of Polydopamine-Modified Carboxymethyl Cellulose Hydrogel for Anti-Recurrence of Tumor. *Colloid. Surf. B* **2021**, *207*, 112025. [CrossRef]
38. Li, W.; Wang, S.; Ren, C.; Liu, P.; Lu, Q.; Yang, L.; Song, Y.; Xu, M.; Tan, F.; Yu, M.; et al. Exo/endogenous Dual-Augmented Chemodynamic Therapy Based on Bioreducible and Bio-breakable Copper (‖)-Based Truncated Octahedron. *Chem. Eng. J.* **2020**, *396*, 125280. [CrossRef]
39. Wang, X.; Zhong, X.; Lei, H.; Geng, Y.; Zhao, Q.; Gong, F.; Yang, Z.; Dong, Z.; Liu, Z.; Cheng, L. Hollow Cu_2Se Nanozymes for Tumor Photothermal-Catalytic Therapy. *Chem. Mater.* **2019**, *31*, 6174–6186. [CrossRef]
40. Cheng, Y.; Zheng, X.; Zhang, L.; Zhao, J.; Hu, L.; Wang, S. Enhanced Photothermal and Chemotherapy of Pancreatic Tumors by Degrading the Extracellular Matrix. *Colloid Surf. B* **2023**, *221*, 113010. [CrossRef]
41. Wang, X.; Zhang, C.; Du, J.; Dong, X.; Jian, S.; Yan, L.; Gu, Z.; Zhao, Y. Enhanced Generation of Non-Oxygen Dependent Free Radicals by Schottky-Type Heterostructures of Au-Bi_2S_3 Nanoparticles via X-Ray-Induced Catalytic Reaction for Radiosensitization. *ACS Nano* **2019**, *13*, 5947–5958. [CrossRef]
42. Voon, S.H.; Kiew, L.V.; Lee, H.B.; Lim, S.H.; Noordin, M.I.; Kamkaew, A.; Burgess, K.; Chung, L.Y. In Vivo Studies of Nanostructure-Based Photosensitizers for Photodynamic Cancer Therapy. *Small* **2014**, *10*, 4993–5013. [CrossRef] [PubMed]
43. Shen, Y.; Liang, L.; Zhang, S.; Huang, D.; Deng, R.; Zhang, J.; Qu, H.; Xu, S.; Liang, C.; Xu, W. Organelle-Targeting Gold Nanorods for Macromolecular Profiling of Subcellular Organelles and Enhanced Cancer Cell Killing. *ACS Appl. Mater. Interfaces* **2018**, *10*, 7910–7918. [CrossRef]
44. Pang, M.; Zeng, H.C. Highly Ordered Self-assemblies of Submicrometer Cu_2O Spheres and Their Hollow Chalcogenide Derivatives. *Langmuir* **2010**, *26*, 5963–5970. [CrossRef]

Disclaimer/Publisher's Note: The statements, opinions and data contained in all publications are solely those of the individual author(s) and contributor(s) and not of MDPI and/or the editor(s). MDPI and/or the editor(s) disclaim responsibility for any injury to people or property resulting from any ideas, methods, instructions or products referred to in the content.